Article

Synthesis of Compliant Parallel Mechanisms Using an Improved Beam-Based Method with the Optimization of Multiple Resonant Modes

Vin Low [1], Song Huat Yeo [1] and Minh Tuan Pham [2,3,*]

1   School of Mechanical and Aerospace Engineering, Nanyang Technological University,
    Singapore 639798, Singapore; vinl0001@e.ntu.edu.sg (V.L.); myeosh@ntu.edu.sg (S.H.Y.)
2   Department of Machine Design, Faculty of Mechanical Engineering, Ho Chi Minh City University of
    Technology (HCMUT), 268 Ly Thuong Kiet Street, District 10, Ho Chi Minh City 700000, Vietnam
3   National University Ho Chi Minh City, Linh Trung Ward, Thu Duc City, Ho Chi Minh City 700000, Vietnam
*   Correspondence: pminhtuan@hcmut.edu.vn

Abstract: This paper proposes an improved beam-based method to synthesize a compliant parallel mechanism (CPM) with multiple degrees of freedom (DoFs). The proposed method utilizes a structural optimization technique to synthesize a three-legged CPM with a single-beam structure constructed by two perpendicular segments in each leg to achieve the desired DoFs and fully decoupled motion. In addition, an objective function is proposed to optimize the primary resonant frequencies in actuating directions to targeted values to achieve the desired dynamic behaviors. A 4-DoF CPM, with one translation and three rotations, is synthesized using the improved beam-based method and all of the primary resonant frequencies are optimized to the targeted values. The 4-DoF CPM prototype is fabricated monolithically and evaluated experimentally in terms of its mechanical characteristics, workspace, and resonant modes. The obtained results show that the experimental stiffness and dynamic properties agree with the predictions. In particular, the prototype has good motion decoupling capability, as reflected by the high stiffness ratios of more than 500 between the non-actuating and actuating directions; the large workspaces of up to 4.0 mm and 7.2° for the translation and rotations, respectively; and the resonant frequencies being close to the targeted ones. In addition, the highest deviations between the predicted and experimental results are 9.49% and 9.13% for the stiffness and dynamic behaviors, respectively, demonstrating the correctness and effectiveness of the proposed method.

Keywords: improved beam-based method; structural optimization; dynamic optimization; decoupled motion; compliant parallel mechanism

1. Introduction

Compliant mechanisms (CMs) are monolithic structures that achieve intended movements via the elastic deformation of flexural links. CMs eliminate the need for parts assembly in conventional rigid mechanisms and are friction- and backlash-free, enabling high precision to be achieved in compact designs [1,2].

The design of CMs can be configured as serial or parallel types [3,4]. CMs designed with a parallel architecture are commonly known as compliant parallel mechanisms (CPMs). CPMs have shorter displacements compared to their serial counterparts but have better performance in terms of their lower inertia, higher stiffness, and dynamic responses, and are less sensitive to external disturbances [5,6]. The ease of implementation of CPMs makes them ideal candidate, and they are favored for high-precision positioning mechanisms [7] with the characteristics of repeatable motion, compactness, amenability, and scalability [8].

Many design methods have been developed for synthesizing CPMs with various degrees of freedom (DoFs) and in different applications, i.e., 1 DoF [9,10] for grippers, 2

DoFs [11,12] for X-Y positioning stages, and 3 to 6 DoFs [13–20] for spatial motion. It is noted that CPMs with 1, 2, 3, and 6 DoFs are more widely developed than those with 4 or 5 DoFs, due to difficulties in the synthesis process.

The existing beam-based method was developed by Pham [21,22] for designing CPMs with decoupled motions, a high stiffness ratio, and large workspaces, with the first resonant mode optimized to a defined value. The method utilized a pair of reflected curved and twisted (C-T) beams to synthesize the leg structure of the CPMs and proposed an objective function to optimize the first resonant frequency for a better dynamic response. Nevertheless, the leg structure with a pair of reflected C-T beams is complex, leading to unnecessarily complicated CPM designs and requiring more computational resources during the synthesis process.

In this paper, an improved beam-based method that overcomes the shortcomings highlighted above is proposed. In addition, a novel dynamic optimization method that considers all primary resonant modes in the actuating directions of CPMs is presented. A single beam with two perpendicular segments is used to synthesize the leg structure of the CPMs via the structural optimization technique. The resultant CPMs will have high stiffness ratios and decoupled motion characteristics. A novel objective function is formulated to optimize the primary resonance frequencies of the actuating directions to the targeted values to achieve the desired dynamic behaviors. Subsequently, a 4-DoF CPM is chosen as a case study, with one translation and three rotations (Z-θ_X-θ_Y-θ_Z), which is synthesized using the improved beam-based method and optimized dynamically. The 4-DoF CPM prototype is fabricated monolithically and evaluated experimentally in terms of its mechanical characteristics, workspace, and resonant modes.

In the following, the design methodology, mathematical formulation, and synthesis of the 4-DoF CPM are described in Section 2. The fabrication and experimental investigation of the prototyped 4-DoF CPM are presented in Section 3. The results and discussion and the conclusions are summarized in Sections 4 and 5, respectively.

2. Design Methodology

2.1. Beam-Based Method

The beam-based method was first proposed by Pham [21,22] for synthesizing multiple-DoF CPMs with a three-legged configuration for positioning systems. In this method, the flexure in each leg is made up by a pair of reflected C-T beams, shown within the cubic design space of the three-legged CPM. The geometry of each C-T beam involves one end being fixed to the ground while the free end is rigidly connected to the moving platform. For decoupled motion CPMs, all beam elements must be distributed in the same plane, and the orientation of the beam must be either horizontal (0°) or vertical (90°), as explained in [22]. Thus, an arbitrary orientation of the C-T beam is not suitable for achieving fully decoupled motions.

Based on the previous literature [22], the beam-based method is unnecessarily complex and the twist angle has been shown to be redundant when synthesizing decoupled motion CPMs. In addition, having a pair of reflected C-T beams is unnecessary and requires more computational resources. Clearly, more materials and longer time periods are also required to fabricate the CPMs, adding to the overall cost. Thus, it can be replaced by a simpler and more effective kind of flexure. This work presents a solution for solving these problems.

2.2. Improved Beam-Based Method with Optimization of Multiple Resonant Modes

The proposed leg structure consists of only a single curved beam with two segments, as shown in Figure 1a. The beam must lie on the X' Y' plane in the design space, and each segment can only have an orientation of either 0° or 90° along the axis of the local frame of the X'' Y'' plane to achieve fully decoupled motion [22], as shown in Figure 1b.
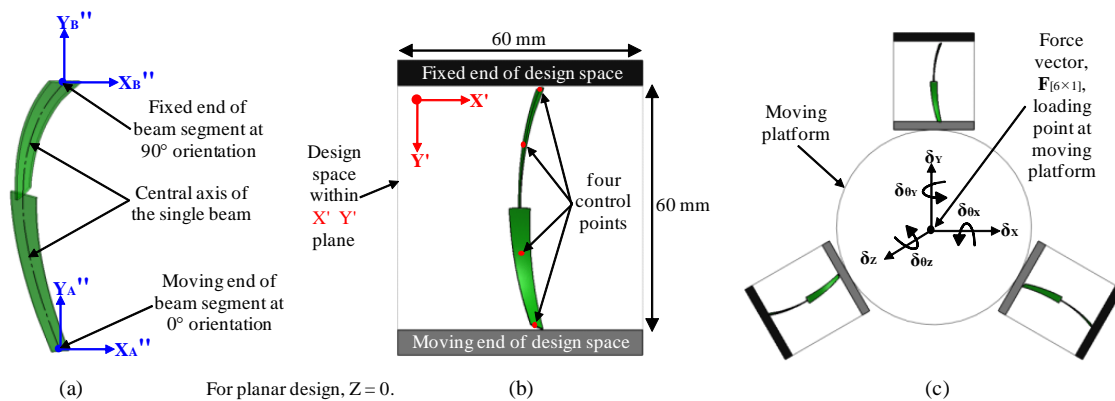
Figure 1. (**a**) Single beam with two perpendicular segments (0° and 90°). (**b**) Design space of a leg. (**c**) Three-legged configuration of the CPM.

A three-legged configuration as shown in Figure 1c is adopted for the synthesis of CPMs with the improved beam-based method. Each leg is formed by the proposed single-beam structure having two perpendicular segments and equally distributed around the moving platform. Note that the principal axes of the cross sections are perpendicular, while the longitudinal axes of the segments are identical. The leg is planar, with one end being fixed to the ground while the other end is rigidly connected to a moving platform. This leg structure is able to perform 6 DoFs at its free end, i.e., three translations (X-Y-Z) and three rotations (θ_X-θ_Y-θ_Z) along and about the X, Y, and Z axes, respectively. The legs are identical, and so only one beam structure in a leg is synthesized during the optimization process.

In modeling the beam for stiffness optimization, a parametric curve (Bezier curve) is used as the center curve of the curved beam, defined by four control points to create the curved profile along the beam structure within the $X'\,Y'$ plane, as shown in Figure 1b. Each control point is defined by its local coordinates $X'_i\,Y'_i$, where i = 1, 2, 3, 4 on the $X'\,Y'$ plane. Hence, there are a total of 8 design variables determining the coordinates of the four control points. Each segment in the beam is represented by a specified number of 2-noded beam elements. Note that the Z''_i values of all control points are set to 0, constraining the beam to be planar. The last design variable during the stiffness optimization is the orientation (can be 0° or 90°) of each beam segment for the CPM to achieve fully decoupled motion. The synthesis procedures of the CPM with the improved beam-based method is shown in Figure 2.
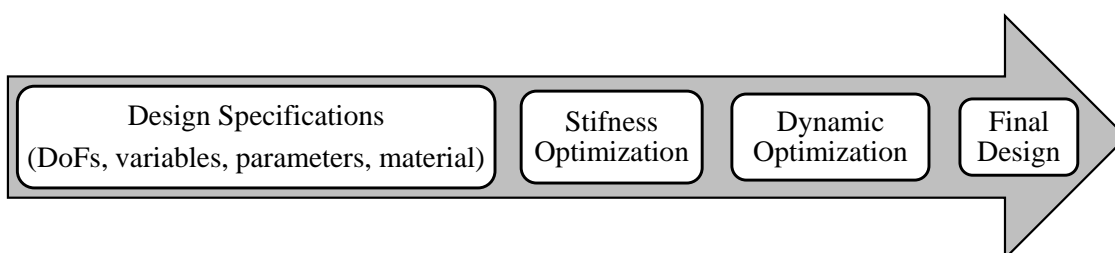

Figure 2. The synthesis procedures of the improved beam-based method.

The design specifications, i.e., the desired DoFs, type of material, and several pre-defined parameters, are first defined. The beam structure in the leg of the CPMs is then obtained from the stiffness optimization process to achieve high stiffness ratios between the non-actuating and actuating ones. Note that the cross-sectional area and the number of beam segments of the single beam are pre-defined in the stiffness optimization process. This is followed by the dynamic optimization process to optimize the resonant modes of the CPMs with the targeted frequencies while keeping the beam compliance as high as possible. There are a total of 4 design variables in the dynamic optimization process, i.e.,

the thickness and diameter of the moving platform and thickness and width of the beam segment. The performance of the synthesized CPM is then verified using a finite element analysis (FEA) via the ANSYS software. Finally, the CPM is fabricated and evaluated experimentally to verify the effectiveness of the proposed method.

2.3. Mathematical Formulation

In this section, two objective functions are formulated to optimize the stiffness and dynamic properties of a general CPM, regardless of its DoFs. For CPMs with a symmetrical configuration, the overall design can be defined by only one leg structure and duplicated across other legs. Each beam structure is meshed by a number of 2-noded beam elements and the finite element method (FEM) is employed for the mechanical behavior to achieve the best possible stiffness and dynamic design for the entire CPM.

In order to better describe the following formulations, the notations used in this work are listed below.

2.3.1. Objective Function for Stiffness Optimization

The aim of the stiffness optimization is to achieve low stiffness along the actuating directions and high stiffness along the non-actuating axes of the CPM. This is because the higher the stiffness, the better the CPM in resisting the external disturbances in the specified directions. Since CPMs deflect by transferring energy from the input to the output through the flexible members, the energy stored in the mechanism is elastic strain energy [23,24]. In the following, the objective function to carry out the stiffness optimization for CPMs is formulated based on the elastic strain energy.

In the FEM, the stiffness matrix size of a 2-noded beam element is 12×12, which is denoted as $\mathbf{K}^b$. The structural stiffness matrix $\mathbf{K}^S$ of the entire CPM with N, the total number of 2-noded beam elements, can be defined as:

$$\mathbf{K}^S = \sum_{p=1}^{N} \mathbf{K}_p^b \tag{1}$$

In general, to obtain the stiffness of the CPM for its 6 DoFs in the moving platform, the static condensation technique in [21,25] is employed to reduce the dimensions of the structural stiffness matrix, $\mathbf{K}^S$, to a 6×6 stiffness matrix, $\mathbf{K}$, as shown in Equation (2):

$$\mathbf{K} = \mathbf{K}_{[6 \times 6]}^S - \mathbf{K}_{[6 \times (S-6)]}^S \cdot \left(\mathbf{K}_{[(S-6) \times (S-6)]}^S \right)^{-1} \cdot \mathbf{K}_{[(S-6) \times 6]}^S \tag{2}$$

Figure 1c shows the moving platform of the CPM being subjected to an external applied force vector, $\mathbf{F}_{[6 \times 1]}$, which has three force components (F_X-F_Y-F_Z) and three moment components (M_X-M_Y-M_Z) along and about the X, Y, and Z axes of the global coordinate system, respectively. The displacement vector, $\boldsymbol{\delta}_{[6 \times 1]}$, consisting of six local components (δ_x, δ_y, δ_z, $\delta_{\theta x}$, $\delta_{\theta Y}$, $\delta_{\theta z}$) corresponding to the applied force vector, can be determined by Hooke's law as follows:

$$\boldsymbol{\delta}_{[6 \times 1]} = \mathbf{C} \cdot \mathbf{F}_{[6 \times 1]} \tag{3}$$

where $\mathbf{C}$ is the compliance matrix of the CPM and $\mathbf{C} = \mathbf{K}^{-1}$.

The strain energy components, U_i and U_j, in the specific directions of the structure stored in the displaced CPM can be obtained using Equations (4) and (5). Let U_i and U_j be the elastic strain energies in the actuating and non-actuating directions of the structure, respectively. The strain energy components, U_i and U_j, are the resultants of the associated force components, F_i and F_j, and the stiffness components, K_i and K_j, respectively:

$$U_i = \frac{1}{2} K_i \delta_i^2 = \frac{1}{2} K_i \left(\frac{F_i}{K_i} \right)^2 = \frac{1}{2} \frac{F_i^2}{K_i} \tag{4}$$

$$U_j = \frac{1}{2}K_j\delta_j^2 = \frac{1}{2}K_j\left(\frac{F_j}{K_j}\right)^2 = \frac{1}{2}\frac{F_j^2}{K_j} \tag{5}$$

where $\delta_i = \frac{F_i}{K_i}$ and $\delta_j = \frac{F_j}{K_j}$ are for decoupled motion CPMs.

In a general CPM, the maximum of 6 DoFs are needed in practical applications. Hence, the relationship between the number of actuating directions (α) and the number of non-actuating directions (β) in a CPM can be expressed as follows:

$$\alpha + \beta = 6 \tag{6}$$

Note that the non-actuating directions are referred to as degrees of constraints (DoCs). In the following formulation, the number of DoFs (i = DoF) and the number of DoCs (j = DoC) for 3 translations (X, Y, Z) are represented by indices 1, 2, and 3 and the 3 rotations (θ_X-θ_Y-θ_Z) by indices 4, 5, and 6, respectively. Let U_i^β be the energy in the actuating directions and U_j^α be the energy in the non-actuating directions. The stiffness property of the CPM can be defined by the total elastic strain energy ratio, R_E, which is defined as the ratio between the product of U_i^β and the product of U_j^α, as shown in Equation (7):

$$R_E = \frac{\prod\limits_{i=1}^{\alpha} U_i^\beta}{\prod\limits_{j=1}^{\beta} U_j^\alpha} \tag{7}$$

Note that $\alpha + \beta = 6$.

Based on the total elastic strain energy ratio, R_E, an objective function, f_s, used to optimize the stiffness property of CPMs is defined as follows:

$$\text{minimize } f_s = \frac{1}{R_E} \tag{8}$$

2.3.2. Objective Function for Optimization of Multiple Resonant Modes

The dynamic response of a CPM determines its ability to withstand mechanical shock or vibration. In this section, an objective function is proposed to optimize the resonance frequencies in the actuating directions to targeted values, thereby achieving the desired dynamic behaviors. The optimization of multiple resonant modes is achieved by optimizing the mass distribution in the structure of a CPM while keeping its stiffness as high as possible compared to those obtained from the stiffness optimization process.

Referring to Equation (9), the mass matrix of a CPM, $\mathbf{M}^S$, can be determined by the summation of the mass of N number of 2-noded beam elements, denoted as $\mathbf{M}^b$, which is a 12×12 matrix:

$$\mathbf{M}^S = \sum_{q=1}^{N} \mathbf{M}_q^b \tag{9}$$

In theory, the formulation for the relationship between the natural frequency and its bandwidth of the entire system matrix size of $S \times 1$ for a CPM [21] denoted as $\mathbf{f}_{[S \times 1]}$ can be derived as shown in Equation (10):

$$\mathbf{f}_{[S \times 1]} = \frac{\boldsymbol{\omega}_{[S \times 1]}}{2\pi} \tag{10}$$

where $\left| -\boldsymbol{\omega}_{[S \times 1]}^2 \cdot \mathbf{M}_{[S \times S]}^S + \mathbf{K}_{[S \times S]}^S \right| = 0$.

Note that full system matrix size $S \times S$ is used in $\mathbf{M}^S$ and $\mathbf{K}^S$ during the dynamic optimization.

The dynamic property of the CPMs can then be optimized by minimizing the objective function f_d as defined in Equation (11):

$$\text{minimize } f_d = \sum_{i=1}^{n}\left(\left|f_i^{\text{targeted}} - f_i\right| - \sum_{\substack{(j=i+1) \\ i<n}}^{n} \frac{f_i}{f_j}\right) \tag{11}$$

In the first term of Equation (11), $\left|f_i^{\text{targeted}} - f_i\right|$ is used to move the natural frequencies of the actuating directions (f_i) close to the targeted values $\left(f_i^{\text{targeted}}\right)$ during the dynamic optimization.

The second term, $\sum_{\substack{j=i+1 \\ i<n}}^{n} \frac{f_i}{f_j}$, is a measure of the gap between the neighboring resonant frequency. Clearly, a smaller neighboring frequency ratio is desirable. The optimized resonant frequencies of the CPM are achieved when the differences between the first and second terms are minimized.

2.4. Synthesis of a 4-DoF (Z-θ_X-θ_Y-θ_Z) CPM

A 4-DoF (Z-θ_X-θ_Y-θ_Z) CPM is synthesized as a case study to evaluate the effectiveness of the proposed method. The synthesis results are obtained by a MATLAB program using the genetic algorithm (GA) solver and then verified using a finite element analysis (FEA) using ANSYS. Referring to Figure 1b, the leg design space is 60 mm × 60 mm, and aluminum alloy 6061 with a Young's modulus of 68.9 GPa, Poisson ratio of 0.33, and yield strength of 276 MPa is selected as the manufacturing material for the CPM. There are 9 design variables to be obtained from the stiffness optimization process and 4 variables are to be obtained from the dynamic optimization process, as described in Section 2.2.

2.4.1. Stiffness Optimization

Equation (8) is used for the stiffness optimization of the 4-DoF CPM with $\alpha = 4$, $\beta = 2$. All forces and moments applied to the CPM platform are assumed to be a unit. As a result, the objective function for the stiffness optimization can be written as shown in Equation (12):

$$\text{minimize } f_s = \frac{K_{\delta_Z}^2 K_{\delta_{\theta_X}}^2 K_{\delta_{\theta_Y}}^2 K_{\delta_{\theta_Z}}^2}{K_{\delta_X}^4 K_{\delta_Y}^4} \tag{12}$$

In Equation (12), the stiffness values in the numerator correspond to the diagonal elements K_{33}, K_{44}, K_{55}, and K_{66} respectively, in the 6 × 6 stiffness matrix **K** of the CPM. Similarly, the stiffness values in the denominator correspond to the diagonal elements K_{11} and K_{22} of **K**, respectively.

Equation (12) is solved using a genetic algorithm in MATLAB and the obtained beam structure design in a leg is illustrated in Figure 3a. It can be seen that the leg design consists of two flat rectangular segments oriented perpendicularly to each other. The stiffness property of the 4-DoF CPM after the stiffness optimization process is represented by $\mathbf{C}_s^{4-\text{DoF}}$ as follows:

$$\mathbf{C}_s^{4-\text{DoF}} = \begin{bmatrix} 4.9912 \times 10^{-7} & 0 & 0 & 0 & 0 & 0 \\ 0 & 4.9912 \times 10^{-7} & 0 & 0 & 0 & 0 \\ 0 & 0 & 7.5489 \times 10^{-4} & 0 & 0 & 0 \\ 0 & 0 & 0 & 1.0640 & 0 & 0 \\ 0 & 0 & 0 & 0 & 1.0640 & 0 \\ 0 & 0 & 0 & 0 & 0 & 2.4068 \times 10^{-1} \end{bmatrix} \tag{13}$$
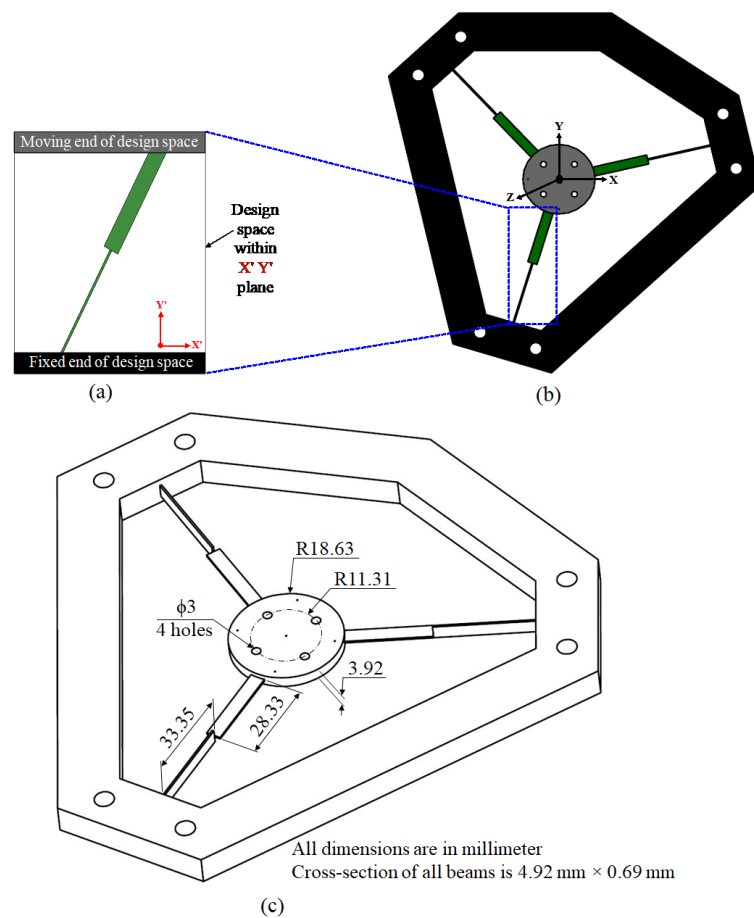
Figure 3. (**a**) The optimal leg structure of a single beam with two perpendicular segments. (**b**) The synthesized 4-DoF CPM with optimized multiple resonant frequencies. (**c**) A 3D model of the CPM with optimized dimensions.

2.4.2. Dynamic Optimization of Multiple Resonant Modes

Equation (11) is optimized with the targeted resonant frequencies $\left(f_i^{\text{targeted}}\right)$, which are chosen as 150 Hz, 400 Hz, 400 Hz, and 500 Hz, being sufficiently high and spaced far enough apart for the 4-DoF CPM in order to verify the effectiveness of the objective function:

$$\text{minimize } f_d = \sum_{i=1}^{4} \left(\left| f_i^{\text{targeted}} - f_i \right| - \sum_{\substack{(j=i+1) \\ i<4}}^{4} \frac{f_i}{f_j} \right) \tag{14}$$

where $i = 3, 4, 5, 6$.

The geometrical values of the optimized beam obtained from the stiffness optimization are used in the dynamic optimization process. Equation (14) enables the optimization of the stiffness and dynamic properties of the 4-DoF CPM design. It is also solved using a genetic algorithm via MATLAB, and the obtained result is represented by a 6×6 compliance matrix, $\mathbf{C}_d^{4-\text{DoF}}$, as shown in Equation (15):

$$\mathbf{C}_d^{4-\text{DoF}} = \begin{bmatrix} 1.7834 \times 10^{-7} & 0 & 0 & 0 & 0 & 0 \\ 0 & 1.7834 \times 10^{-7} & 0 & 0 & 0 & 0 \\ 0 & 0 & 9.4357 \times 10^{-5} & 0 & 0 & 0 \\ 0 & 0 & 0 & 1.4160 \times 10^{-1} & 0 & 0 \\ 0 & 0 & 0 & 0 & 1.4160 \times 10^{-1} & 0 \\ 0 & 0 & 0 & 0 & 0 & 3.0713 \times 10^{-2} \end{bmatrix} \tag{15}$$

2.4.3. Discussion of the Optimized Results

The synthesized leg structure, obtained from the stiffness optimization process, consists of only a single beam made up of two perpendicular rectangular segments, as shown in Figure 3a. One segment oriented at 90° is fixed to the base and the other beam segment at 0° is connected to the moving end. The geometrical values of the beams are used in the dynamic optimization to obtain the final sizes of the leg structure and the moving platform. Figure 3b shows the synthesized three-legged 4-DoF CPM with a circular platform and Figure 3c shows a detailed 3D model of the synthesized CPM with the optimized dimensions obtained after the optimization processes.

When the flexures of a CPM deform, this can reduce the accuracy of the desired output motions. In theory, any parasitic motion will be reflected in the non-diagonal components of the stiffness or compliance matrix of the CPM, which will create undesired motions that reduce the accuracy of the output motions at the moving platform of the CPM. Hence, a decoupled motion characteristic is desirable in the design of CPMs for precision positioning systems. Here, it is noted that all off-diagonal elements in the compliance matrices of the synthesized CPM are zeros, as written in Equations (13) and (15). This theoretically suggests that the 4-DoF CPM is capable of achieving fully decoupled motions.

The motion decoupling capability of a CPM can also be reflected by the stiffness ratios between the actuating and non-actuating directions. A high stiffness ratio implies that the actuating direction is more flexible while the non-actuating direction is stiff, thereby being able to resist the external mechanical disturbance [21,26]. The synthesized CPM has motion decoupling capability, as demonstrated by its diagonal compliance matrix shown in Equation (15). In particular, the output motions of the CPM are fully decoupled without impacting each other. The diagonal components in Equation (15) suggest that the stiffness ratios for the translational directions are greater than 500, as shown in Equation (16). This obtained stiffness ratio is very high, as the non-actuating direction of the CPM is at least of 500 times stiffer than the actuating directions. Note that there is no stiffness ratio for the rotational directions, as all rotations are the DoFs of the CPM:

$$\frac{K_{\delta_X}}{K_{\delta_Z}} = \frac{K_{\delta_Y}}{K_{\delta_Z}} = \frac{C_{\delta_Z}}{C_{\delta_X}} = \frac{C_{\delta_Z}}{C_{\delta_Y}} = \frac{9.4357 \times 10^{-5}}{1.7834 \times 10^{-7}} = 529.08 \tag{16}$$

The compliance results from MATLAB (predicted) are compared with those obtained from the FEA software, as shown in Table 1. It can be seen that there is good agreement, as the deviation is within 5%. Hence, the predicted compliance results are reliable and will be used for a comparison with the experimental results.

Table 1. Deviation of the compliance results: FEA vs. predicted.

Actuating Direction of Compliance	(a) Predicted Compliance (m/N) or (rad/Nm)	(b) FEA Compliance (m/N) or (rad/Nm)	% Deviation (b) vs. (a)
along Z-axis	9.4357×10^{-5}	9.3690×10^{-5}	0.71
about Z-axis	3.0713×10^{-2}	3.2097×10^{-2}	4.51
about X-axis	1.4160×10^{-1}	1.4339×10^{-1}	1.27
about Y-axis	1.4160×10^{-1}	1.4373×10^{-1}	1.29

Table 2 shows the targeted resonant frequencies of actuating directions, denoted by f_I^{targeted} in Equation (14), along with the resonant frequencies obtained after the dynamic optimization (represented by the predicted values) and the FEA resonant frequencies obtained via the ANSYS simulation. Moreover, the deviations between the optimized results and other values are also presented. It can be seen that the deviations between the targeted and predicted frequencies are within 3%, showing the effectiveness of the proposed objective function in optimizing multiple resonant modes. The deviations between the

predicted and FEA results are below 7% accuracy. Therefore, the predicted result in Table 2 will be used for comparison with the experimental results.

Table 2. Deviations of the resonant frequency results: predicted versus targeted and FEA.

Actuating Direction of Resonant Frequency	(a) Targeted Resonant Frequency (Hz)	(b) Predicted Resonant Frequency (Hz)	(c) FEA Resonant Frequency (Hz)	% Deviation (b) vs. (a)	% Deviation (b) vs. (c)
along Z-axis	150	149.15	152.70	0.52	2.38
about Z-axis	500	514.25	478.40	2.85	6.97
about X-axis	400	409.07	400.97	2.27	1.98
about Y-axis	400	409.07	400.77	2.27	2.03

The workspace of the 4-DoF CPM is obtained from the FEA software as shown in Table 3. It can be seen that the range of linear motion along the Z-axis is ± 2.0 mm, while the ranges of rotational motions about the X-, Y-, and Z-axis are $\pm 3.6°$, $\pm 3.6°$, and $\pm 2.0°$, respectively. The workspace will be used as a reference during the experimental investigation to displace the CPM within the ranges.

Table 3. The workspace of the synthesized 4-DoF CPM verified by the FEA.

Actuating Direction of Compliance	along Z-Axis	about X-Axis	about Y-Axis	about Z-Axis
Full workspace	4.0 mm (± 2.0 mm)	7.2° ($\pm 3.6°$)	7.2° ($\pm 3.6°$)	4.0° ($\pm 2.0°$)

In summary, it has been shown that the deviations of both the compliances and resonant frequencies are below 7%. These small deviations illustrate that the 4-DoF CPM design is viable. Therefore, the synthesized 4-DoF CPM will be fabricated and its performance will be investigated via experiments to evaluate the effectiveness of the proposed method.

2.4.4. Formulation of the Pseudo-Rigid Body Model (PRBM)

The compliance results in Tables 1 and 2 are for small displacements along the linear stiffness region, which can be verified using the FEA effectively. However, the CPM design is under over-constraint conditions, as the platform is being connected by three parallel legs clamped at both ends. As such, it will be experiencing both the linear and non-linear stiffness behaviors in the compliance experiment. The PRBM is used to predict the non-linear stiffness behavior for large displacements [27,28].

The PRBM is formulated based on the fixed clamped beam model from the literature [27–30]. The parameters [27,28] indicated in Figure 4 are used to derive Equation (17). The diagonal stiffness components in Equation (15) are used to derive the axial force per unit strain, EA, and the beam flexure rigidity, EI, in each actuating direction of the CPM. The unitless characteristic radius, γ, and the unitless bending stiffness coefficient, K_θ, are selected as 0.85 and 2.65 from the literature [28–30], respectively. Both selected parameters, γ and K_θ, are suitable in the PRB model with fixed-clamped condition, and are subjected to tensile force applications. Here, γ is consistent for large displacement, while K_θ has a small impact on the modeling, as explained in [28]. The selected γ and K_θ parameters are commonly used in the PRBM, as reported in [29,30].

$$F = 3\left[\frac{K_A \Delta L \delta}{\gamma L + \Delta L} + \frac{2K_T \theta}{\gamma L \cos\theta} \right] \tag{17}$$

where:

$$K_A = \frac{(EA)_{\text{Axial}}}{(\gamma L + \Delta L)}; \ \Delta L = \sqrt{\delta^2 + (\gamma L)^2} - \gamma L; \ \delta = \gamma L \sin\theta; \ K_T = 2\frac{\gamma}{L} K_\theta (EI)_{\text{Bending}}; \ \text{and}$$
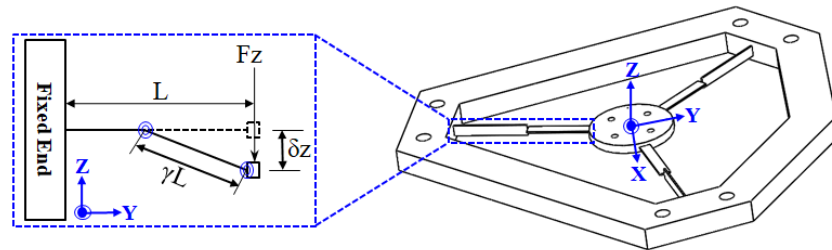$$\theta = \tan^{-1}\left(\frac{\delta}{\gamma L}\right)$$

Figure 4. The parameters for the curve predicted by the PRBM.

In Equation (17), the first force component term is associated with the stiffness of the linear spring, K_A, incremental beam length, ΔL, displacement, δ, and the original beam length, L. The second force component is associated with the stiffness of the torsion spring, K_T, angle of the displacement, θ, and original beam length, L.

3. Experimental Investigation of a 4-DoF CPM Prototype

In this section, experiments to evaluate the actual compliance and dynamic characteristics of the 4-DoF CPM are presented. In particular, experiments were conducted to obtain the workspaces and resonant frequencies of the prototyped 4-DoF CPM in the four actuating directions (Z-θ_X-θ_Y-θ_Z). Due to the over-constraint design of the CPM, non-linear stiffness behaviors will occur in the compliance experiment. The non-linear region can be described by the PRBM formulated and presented in Section 2.4.4.

3.1. Fabrication and Compensation of the Prototype

The prototype of the 4-DoF CPM was made using aluminum alloy 6061. It was fabricated using a combination of wire-cut and CNC milling. The fabricated leg has a single beam with two perpendicular segments, as shown in Figure 5a. The entire 4-DoF (Z-θ_X-θ_Y-θ_Z) CPM was monolithically fabricated, as shown in Figure 5b. The moving platform of the CPM, shown in Figure 5c, has four holes for mounting a test fixture (additional mass) during the dynamic experiment. The material removed from the four holes reduces the design mass of the platform and can affect the result of the dynamic experiment. Therefore, the mass of the platform needs to be compensated. In addition, the surface of the moving platform is designed with the specific points, which are the locations for applying forces when conducting the compliance experiment.
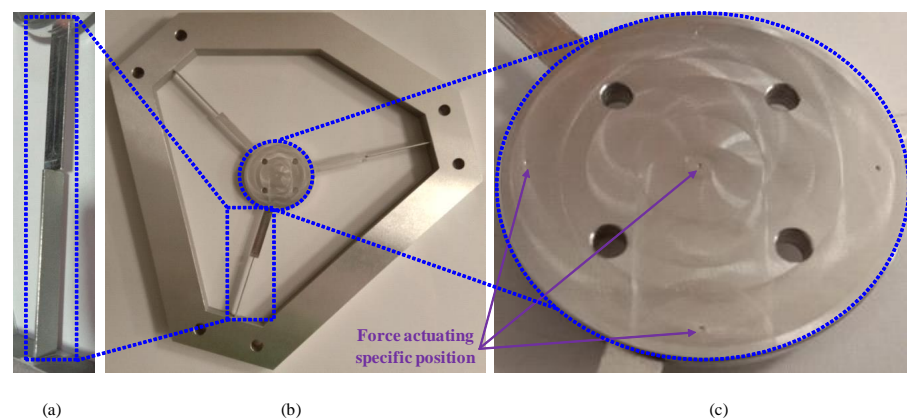

Figure 5. (**a**) A single beam with two perpendicular segments. (**b**) The prototype of the 4-DoF CPM. (**c**) The specific points for force actuating on the moving platform.

3.2. Experiments to Evaluate the Compliance of the Prototype

The setups of the compliance experiment along the Z-axis, about the Z-axis, about the X-axis, and about the Y-axis are shown in Figure 6a–d, respectively. A force sensor (LCM DCE-100N) is used to measure the actuating forces. A rigid rod with a sharp, pointed tip is connected to the force sensor, allowing the force to be applied at the specific position. The input displacement is produced using a micrometer with a resolution of 1.25 μm. The magnitude of the actuating force is shown on a digital display.
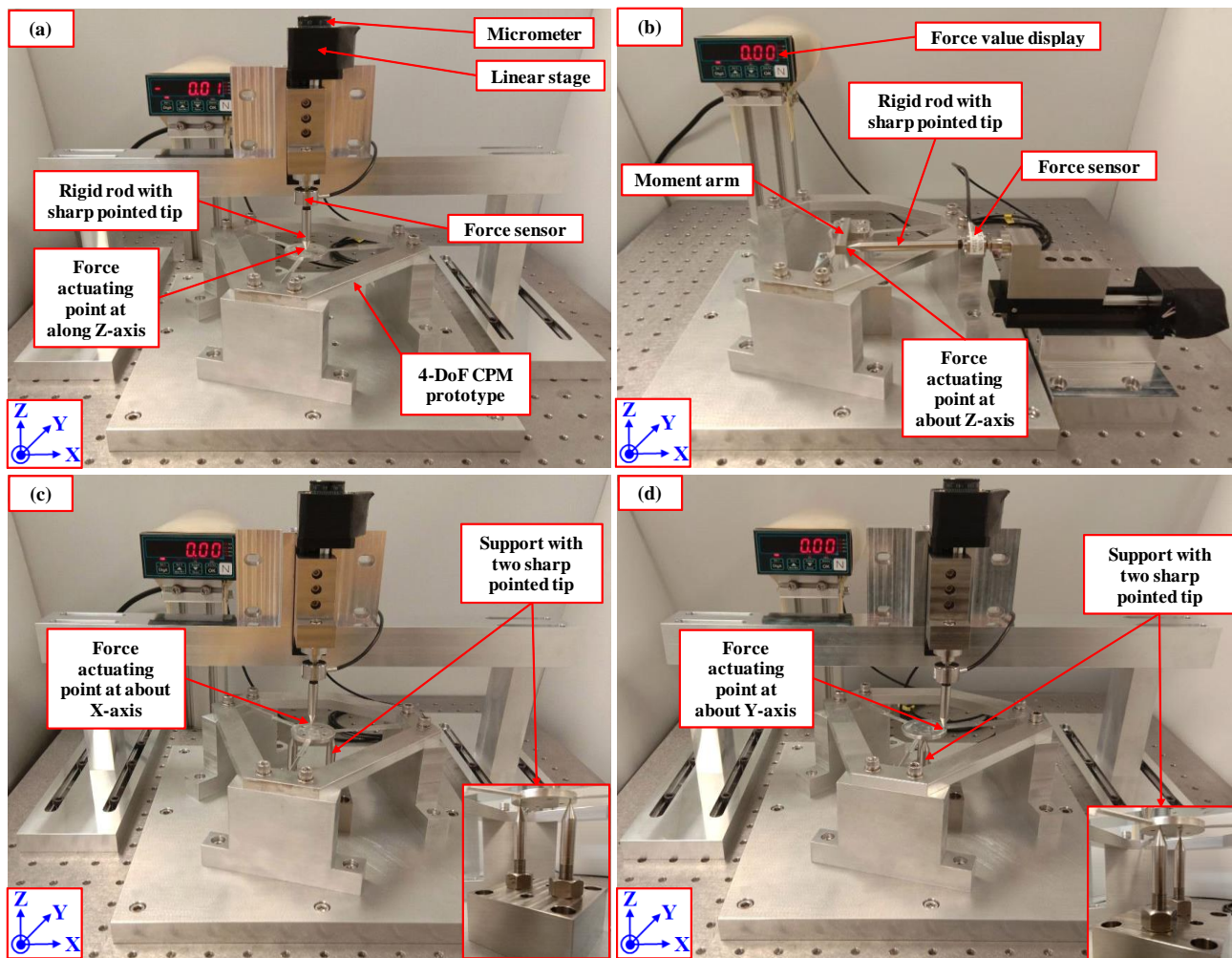

Figure 6. Experimental setup for compliance verification: (**a**) along the Z-axis; (**b**) about the Z-axis; (**c**) about the X-axis; (**d**) about the Y-axis.

For the experiment shown in Figure 6a, the micrometer moves the rigid rod towards the moving platform, thereby creating an input displacement and an applied force. The displacements and the forces obtained are used to calculate the compliance along the Z-axis.

For the compliance experiment about the Z-axis, as shown Figure 6b, a rotational cylinder support is placed at the bottom of the moving platform to create pure rotation at about Z-axis. Both the platform and the support are secured by screws in the four holes. This is to ensure that pure rotation about the Z-axis is generated. The moment arm mounted on the top of the platform enables the rigid rod to contact at specific point to produce the desired input moment about the Z-axis.

For the compliance experiments about the X- and Y-axes, as illustrated in Figure 6c,d, a set of two sharp pointed tips is used as a support below the platform. The support ensures that the rotation is purely about the axis of interest when the rigid rod moves close to the platform.

The experimental results obtained from the compliance experiments are plotted as shown in Figure 7. Note that each experiment was conducted over the workspace of the CPM and repeated five times for each actuating direction to ensure the repeatability and reliability of the experimental results. In addition, the full working ranges of the CPM as shown in Table 3 were also experimentally verified.
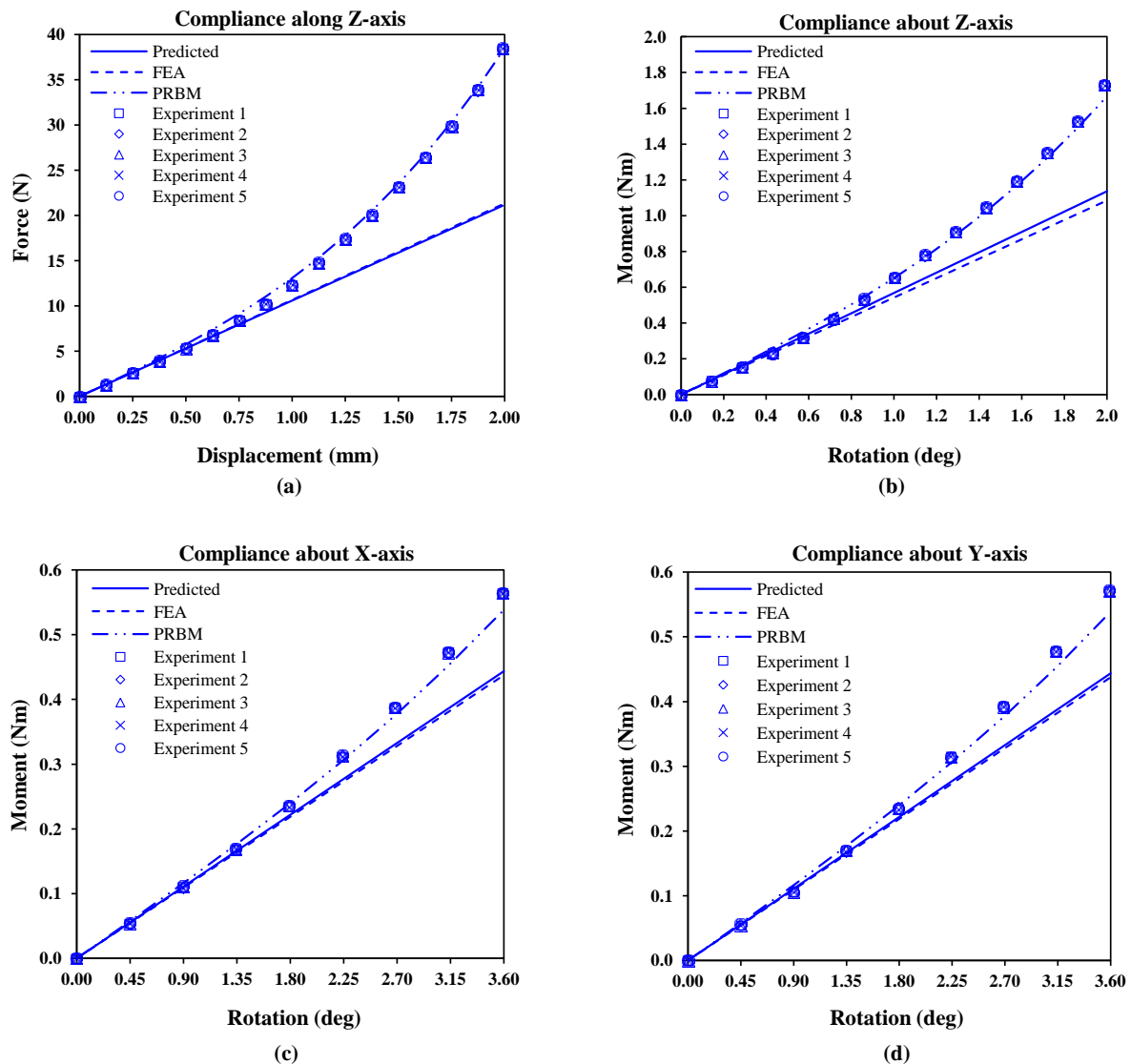

Figure 7. Experimental results plotted against the predicted, FEA, and PRBM results: (**a**) along the Z-axis; (**b**) about the Z-axis; (**c**) about the X-axis; (**d**) about the Y-axis.

Referring to Figure 7, it can be seen that for all actuating directions, the experimental curves exhibit a linear relationship over a small range of displacements and become non-linear subsequently. Table 4 shows a comparison of the compliance between the experimental results and predicted values from the FEM over the linear ranges. The deviations are below 10%, with the highest being 9.49% for translation along the Z-axis and the lowest being 3.95% for rotation about the Y-axis.

For the non-linear ranges, the experimental results are compared with the PRBM values obtained based on Equation (17). The deviations are below 5%, with the highest being 4.81% for translation along the Z-axis and the lowest being 1.23% for rotation about the X-axis as shown in Table 5.

Table 4. Deviations in the experimental results compared to the predicted results along the linear range.

Actuating Direction of Compliance	(a) Predicted Compliance (m/N) or (rad/Nm)	(b) Average Experimental Compliance (m/N) or (rad/Nm)	% Deviation (b) vs. (a)
along Z-axis from 0–1 mm	9.4357×10^{-5}	8.5399×10^{-5}	9.49
about Z-axis from 0–1°	3.0713×10^{-2}	2.8111×10^{-2}	8.47
about X-axis from 0–1.8°	1.4160×10^{-1}	1.3528×10^{-1}	4.46
about Y-axis from 0–1.8°	1.4160×10^{-1}	1.3601×10^{-1}	3.95

Table 5. Deviations in the experimental results compared to the PRBM results along the non-linear range.

Actuating Direction of Compliance	(a) Average Experimental Compliance (m/N) or (rad/Nm)	(b) Average PRBM Compliance (m/N) or (rad/Nm)	% Deviation (b) vs. (a)
along Z-axis from 1 mm onward	7.9744×10^{-5}	7.6086×10^{-5}	4.81
about Z-axis from 1° onward	2.6389×10^{-2}	2.6731×10^{-2}	1.28
about X-axis from 1.8° onward	1.3244×10^{-1}	1.3083×10^{-1}	1.23
about Y-axis from 1.8° onward	1.3267×10^{-1}	1.3083×10^{-1}	1.41

The deviations can be caused by manufacturing errors in the CNC machining processes. It can be concluded that the effectiveness of the proposed improved beam-based method in synthesizing compliant parallel mechanisms (CPMs) with multiple degrees of freedom (DoFs) has been demonstrated by the experimental results.

From the experimental compliance results, as mentioned above, the stiffness property of the prototyped 4-DoF CPM is predictable in both linear and non-linear ranges. This demonstrates the correctness of the stiffness optimization results and the PRBM.

3.3. Experiments to Evaluate the Dynamic Response of the Prototype

The dynamic experiments were performed to evaluate the dynamic response of the prototyped 4-DoF (Z-θ_X-θ_Y-θ_Z) CPM. The setup of the dynamic experiments is shown in Figure 8. A standard modal analysis instrument is used in the experiments to capture the frequency response of the CPM. An impact hammer provides excitation to the platform of the CPM prototype. The acceleration from the platform is detected by an accelerator attached to the platform. The acceleration is transmitted as an input signal to the frequency response function (FRF) software, which analyzes the input signal and displays the frequency response in Hz.

It should be highlighted that there is a change of geometry in the transitional positions in corners, such as those between the two perpendicular segments of the beam, caused by the tool radius during CNC milling. The mass of the CPM prototype increases as a result due to the rounding radius at the interface. In addition, a test fixture is mounted on the moving platform of the CPM to assess the dynamic response about the Z-axis, as shown in Figure 8. This additional mass (~9.5 g) can affect the dynamic behavior of the CPM prototype, and so it must be compensated for in the determination of the predicted resonant frequencies. All of the mentioned aspects are considered to recalculate the dynamic behaviors of the actual CPM, and the compensated resonant frequencies of the physical prototype are shown in Table 6. Note that the values in Table 6 will be used as predicted frequencies for comparison with the experimental results.
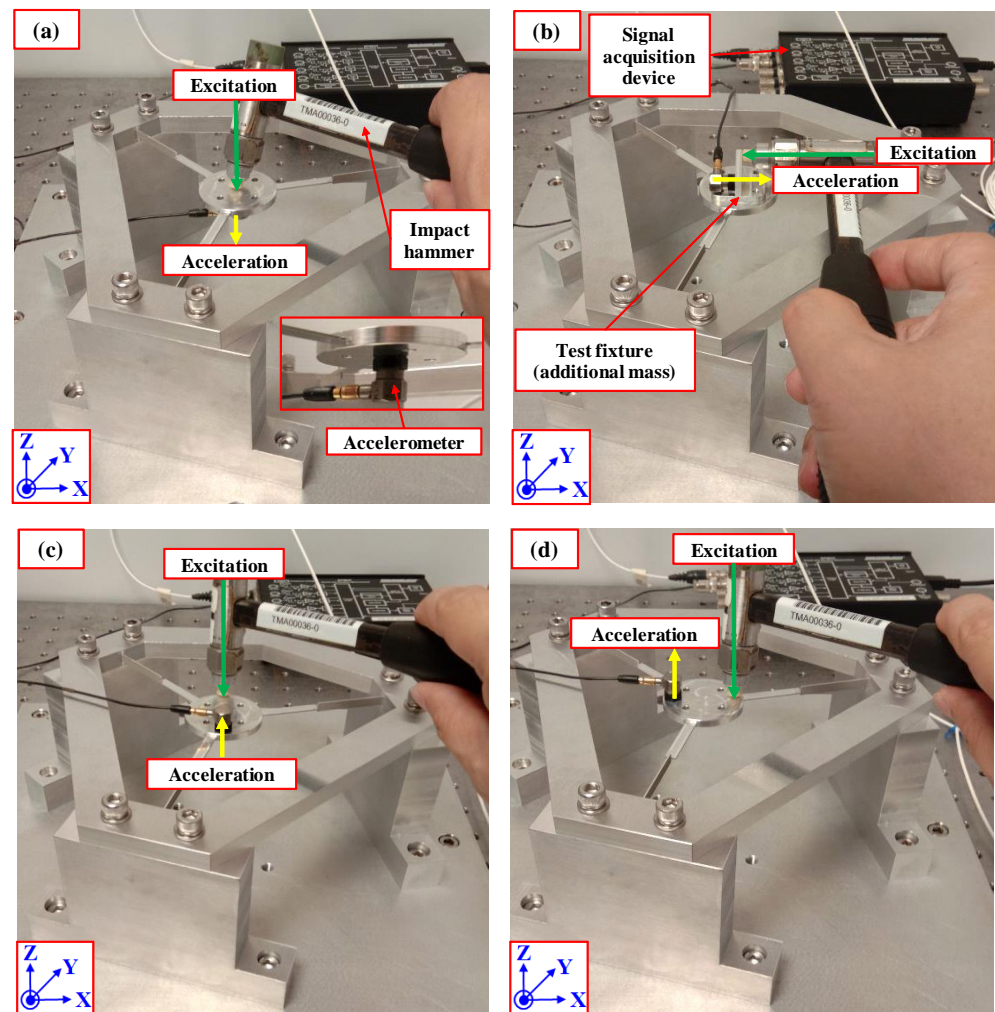
Figure 8. Experimental setups for dynamic responses: (**a**) along the Z-axis; (**b**) about the Z-axis; (**c**) about the X-axis; (**d**) about the Y-axis.

Table 6. Compensated resonant frequencies.

Actuating Direction of Resonant Frequency	along Z-Axis	about Z-Axis	about X-Axis	about Y-Axis
Compensated resonant frequency (Hz) by FEA	124.9	319.1	331.7	326.2

Figure 8a shows the setup for the dynamic response along the Z-axis with the accelerator attached below the platform. The input excitation is generated by the impact hammer along the Z-axis.

Figure 8b shows the setup for the dynamic response about the Z-axis with a test fixture mounted on the moving platform of the prototype. The accelerator is attached on one side of the test fixture. The excitation is horizontally applied on the other side of the test fixture. Note that the dynamic response about the Y-axis will also be captured simultaneously due to the direction of excitation.

Figure 8c,d show the setups for the dynamic responses about the X- and Y- axes. The excitation is applied vertically downward on the edge of the platform with the acceleration attached diagonally at the other edge. The dynamic response along the Z-axis is also captured in this measurement. This is due to the downward motion of the platform when excitation is applied at edge of the platform when generating rotation about the X- or Y-axis.

The frequency responses obtained from the experiments are shown in Figure 9. The experimental resonant frequencies in the actuating directions along the Z-axis and about the X-, Y-, and Z- axes, as well as the deviations between the experimental results and

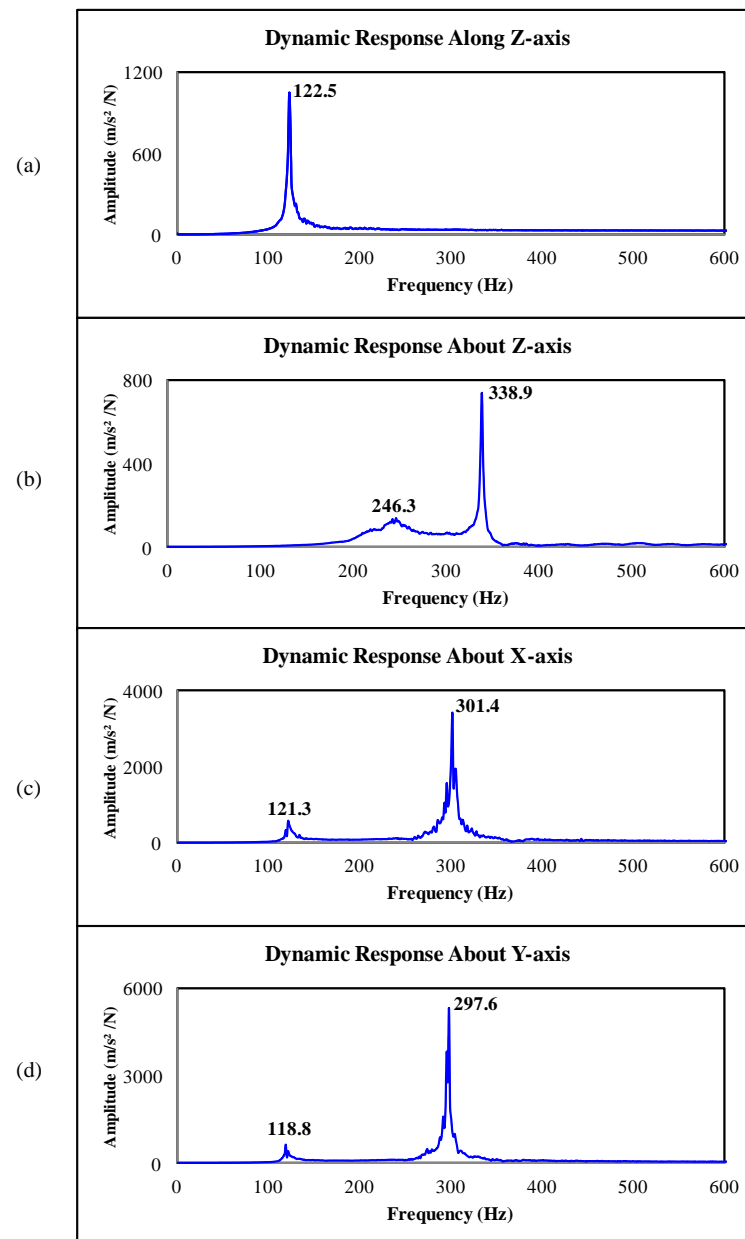predicted values, are listed in Table 7. The highest deviation is 9.13% about the X-axis in this experiment.

Figure 9. Experimental results of the dynamic responses: (**a**) along the Z-axis; (**b**) about the Z-axis; (**c**) about the X-axis; (**d**) about the Y-axis.

Table 7. Deviations of the experimental resonant frequencies compared to the FEA compensated results.

Actuating Direction of Resonant Frequency	(a) Compensated Resonant Frequency (Hz) by FEA	(b) Experimental Resonant Frequency (Hz)	% Deviation of (a) and (b)
along Z-axis	124.9	122.5	1.92
about Z-axis	319.1	338.9	6.20
about X-axis	331.7	301.4	9.13
about Y-axis	326.2	297.6	8.77

From Figure 9a, it can be seen that the experimental resonance frequency along the Z-axis is 122.5 Hz. This resonance frequency also appears in Figure 9c,d, with values of 121.3 Hz and 118.8 Hz, respectively. This is because the moving platform also experiences excitation along the Z-axis when the rotation about the X- or Y-axis is excited. The frequency of 122.5 Hz from this experiment, which is the value obtained by the direct measurement, will be used for comparison.

Referring to Figure 9b, the resonant frequency about the Z-axis is 338.9 Hz. As highlighted above, the other peak with a value 246.3 Hz corresponds to that about the Y-axis.

From Figure 9c,d, the resonant frequencies about the X- and Y- axes are 301.4 Hz and 297.6 Hz, respectively. It is noted that the resonant frequency of 297.6 Hz about the Y-axis differs greatly from the 246.3 Hz captured in Figure 9b. This is due to the additional mass of the test fixture in the experimental setup for the dynamic response about the Z-axis. Therefore, the value of 297.6 Hz will be used for comparison, as it is the direct measurement value.

4. Discussion

In this work, a 4-DoF CPM, with one translation and three rotations, was synthesized using the improved beam-based method and all of the primary resonance frequencies were optimized to the targeted values. Note that designing a fully parallel CPM with decoupled motion to achieve the required 4-DoF is not a simple task, and the design in [15] was a hybrid parallel–serial configuration. Another 4-DoF (3R1T) CPM in [16] was not capable of motion decoupling and the development occurred at the simulation stage only.

The 4-DoF CPM prototype was fabricated monolithically and evaluated experimentally in terms of its stiffness, workspace, and resonant modes. The obtained results show that the experimental stiffness and dynamic properties agree with the predictions. In particular, the prototype has a stiffness ratio greater than 500 in the translation direction, considerably higher than the stiffness ratio of 29 reported in [31] for the same translation direction. The high stiffness also reflects the good motion decoupling of the 4-DoF CPM prototype.

The merits of this proposed method are its simple leg structure for the synthesis of CPMs and the formulation of the objective function to achieve the optimization of multiple resonance modes. The single beam design reduces the computational resources and the objective function enables the optimization of dynamic responses with targeted resonant frequencies. The proposed method overcomes the shortcomings of the existing beam-based method [21,22] of having a pair of reflected beam structures and optimizes the dynamic response to only the first resonant mode. Therefore, the objective of this work was achieved.

5. Conclusions

Based on the obtained results, there are two main contributions in this paper. The first is the proposed design of a simple leg structure with two segments oriented at $0°$ or $90°$ in a single beam. The single-beam geometry is simpler, more flexible, and eliminates the complexity of the existing beam-based design with a pair of reflected beams. The second is the formulation of an objective function for the optimization of multiple resonant modes. It should be highlighted that the proposed objective function for the dynamic optimization of multiple resonant modes is a significant contribution, enabling the optimization of multiple dynamic responses to the desired resonant modes.

The effectiveness of the proposed method was verified by a 4-DoF CPM prototype (Z-θ_X-θ_Y-θ_Z). From the experimental results, the prototype has been shown to have fully decoupled motion, high stiffness ratios > 500, a large workspace of 4.0 mm $\times$ 7.2° $\times$ 7.2° $\times$ 4.0°, and resonant modes of 122.6 Hz $\times$ 301.4 Hz $\times$ 297.6 Hz $\times$ 338.9 Hz, as targeted in the actuating directions. The differences between the predicted results and experimental ones are less than 10%. Hence, the improved beam-based synthesis method and the dynamic optimization process for multiple resonant frequencies are valid and effective.

Our future research work will continue to improve the synthesis method by including the stress modeling in the optimization processes to define the stress distribution within

the structure and to determine the workspace of CPMs more accurately. In addition, the improved beam-based method will be applied to develop more CPM designs with various DoFs and targeted dynamic characteristics.

Abbreviation

Notations	Meaning	Equation That the Notations Appear
$\boldsymbol{\delta}/\delta$	Displacement vector/displacement component	(3), (4), (5)
γ	Characteristic radius	(17)
$\boldsymbol{\omega}$	Angular frequency vector	(10)
$\mathbf{C}/C$	6×6 compliance matrix of the CPM/diagonal compliance component of the CPM	(3), (16)
$\mathbf{C}_d$	6×6 compliance matrix after dynamic optimization	(15)
$\mathbf{C}_S$	6×6 compliance matrix after stiffness optimization	(13)
$\mathbf{F}/F$	Force vector/force component	(3), (4), (5)
$\mathbf{f}$	Resonant frequency vector	(10)
f_d	Objective function for dynamic optimization	(11), (14)
f_S	Objective function for stiffness optimization	(8), (12)
f^{targeted}	Targeted resonant frequency	(11), (14)
$\mathbf{K}/K$	6×6 stiffness matrix of the CPM/diagonal stiffness component of the CPM	(2), (4), (5), (12), (16)
$\mathbf{K}^b$	12×12 stiffness matrix of a 2-noded beam element	(1)
$\mathbf{K}^S$	Full stiffness matrix of the entire CPM	(1), (2), (10)
K_A	Stiffness of the linear spring	(17)
K_T	Stiffness of the torsion spring	(17)
K_θ	Bending stiffness coefficient	(17)
$L/\Delta L$	Original beam length/change of length	(17)
$\mathbf{M}^b$	12×12 mass matrix of a 2-noded beam element	(9)
$\mathbf{M}^S$	Full mass matrix of the entire CPM	(9), (10)
R_E	Total elastic energy ratio	(7)
U	Strain energy of the CPM	(4), (5), (7)

References

1. Zhan, W.; He, X.; Yang, J.; Lai, J.; Zhu, D. Optimal design method for 3-DOF planar compliant mechanisms based on mapping matrix constraints. *Structures* **2020**, *26*, 1–5. [CrossRef]
2. Hao, G. Towards the design of monolithic decoupled XYZ compliant parallel mechanisms for multi-function applications. *Mech. Sci.* **2013**, *4*, 291–302. [CrossRef]
3. Ling, M.; Cao, J.; Howell, L.L.; Zeng, M. Kinetostatic modeling of complex compliant mechanisms with serial-parallel substructures: A semi-analytical matrix displacement method. *Mech. Mach. Theory* **2018**, *125*, 169. [CrossRef]
4. Zhang, Y.; Su, H.-J.; Liao, Q. Mobility criteria of compliant mechanisms based on decomposition of compliance matrices. *Mech. Mach. Theory* **2014**, *79*, 80–93. [CrossRef]
5. Teo, T.J.; Yang, G.; Chen, I.-M. Compliant manipulators. In *Handbook of Manufacturing Engineering and Technology*; Nee, A.Y.C., Ed.; Springer: London, UK, 2015; Volume 4, pp. 2229–2300. [CrossRef]
6. Jung, H.K.; Crane, C.D., III; Roberts, R.G. Stiffness mapping of compliant parallel mechanisms in a serial arrangement. *Mech. Mach. Theory* **2008**, *43*, 271–284. [CrossRef]
7. Wu, X.; Lu, Y.; Duan, X.; Zhang, D.; Deng, W. Design and DOF Analysis of a Novel Compliant Parallel Mechanism for Large Load. *Sensors* **2019**, *19*, 828. [CrossRef]
8. Mankame, N.D.; Ananthasuresh, G.K. Topology optimization for synthesis of contact-aided compliant mechanisms using regularize contact modeling. *Comput. Struct.* **2004**, *82*, 1267–1290. [CrossRef]
9. Wang, J.-Y.; Lan, C.-C. A Constant-Force Compliant Gripper for Handling Objects of Various Sizes. *J. Mech. Des.* **2004**, *136*, 071008. [CrossRef]
10. Liu, C.-H.; Huang, G.-F.; Chiu, C.-H.; Pai, T.-Y. Topology Synthesis and Optimal Design of an Adaptive Compliant Gripper to Maximize Output Displacement. *J. Intell. Robot. Syst.* **2018**, *90*, 287–304. [CrossRef]
11. Zhu, W.-L.; Zhu, Z.; Shi, Y.; Wang, X.; Guan, K.; Ju, B.-F. Design, modeling, analysis and testing of a novel piezo-actuated XY compliant mechanism for large workspace nano-positioning. *Smart Mater. Struct.* **2016**, *25*, 115033. [CrossRef]
12. Zhu, W.-L.; Zhu, Z.; Guo, P.; Ju, B.-F. A novel hybrid actuation mechanism based XY nanopositioning stage with totally decoupled kinematics. *Mech. Syst. Signal Process.* **2018**, *99*, 747–759. [CrossRef]
13. Wang, R.; Zhang, X. Optimal design of a planar parallel 3-DOF nanopositioner with multi-objective. *Mech. Mach. Theory* **2017**, *112*, 61–83. [CrossRef]
14. Guo, Z.; Tian, Y.; Liu, C.; Wang, F.; Liu, X.; Shirinzadeh, B.; Zhang, D. Design and control methodology of a 3-DOF flexure-based mechanism for micro/nano-positioning. *Robot. Comput. Integr. Manuf.* **2017**, *32*, 93–105. [CrossRef]
15. Pinskier, J.; Shirinzadeh, B.; Clark, L.; Qin, Y. Development of a 4-DOF haptic micromanipulator utilizing a hybrid parallel-serial flexure mechanism. *Mechatron.* **2018**, *50*, 55–68. [CrossRef]
16. Zhu, D.; Zhan, W.; He, X. Design Method of Three-Rotation and Translation Spatial Full Compliant Mechanism. *IOP Conf. Ser: Mater. Sci. Eng.* **2018**, *423*, 012039. [CrossRef]
17. Gupta, V.; Perathara, R.; Chaurasiya, A.K.; Khatait, J.P. Design and analysis of a flexure based passive gripper. *Precis Eng.* **2019**, *56*, 537–548. [CrossRef]
18. Zhou, Y.; Sun, J.; Zhang, F.; Li, S. Synthesis method of new weakly-coupled 5-DOF compliant parallel mechanism. *J. Mech. Sci.* **2019**, *36*, 3863–3873. [CrossRef]
19. Chen, S.-C.; Culpepper, M.L. Design of a six-axis micro-scale nanopositioner—μHexFlex. *Precis Eng.* **2006**, *30*, 314–324. [CrossRef]
20. Lin, S.; Wang, J.; Xiong, W.; Hu, Q.; Liu, H.; Wang, Q. Design and Modeling of a Curved Beam Compliant Mechanism with Six Degrees of Freedom. *Micromachines* **2022**, *13*, 208. [CrossRef]
21. Pham, M.T.; Teo, T.J.; Yeo, S.H. Synthesis of multiple degrees-of-freedom spatial-motion compliant parallel mechanisms with desired stiffness and dynamics characteristics. *Precis Eng.* **2017**, *47*, 131–139. [CrossRef]
22. Pham, M.T.; Yeo, S.H.; Teo, T.J.; Wang, P.; Nai, M.L.S. Design and Optimization of a Three Degrees-of-Freedom Spatial Motion Compliant Parallel Mechanism with Fully Decoupled Motion Characteristics. *J. Mech. Robot.* **2019**, *11*, 051010. [CrossRef]
23. Gallego, J.A.; Herder, J. Criteria for the static balancing of compliant mechanisms. In Proceedings of the ASME 2010 International Design Engineering Technical Conferences and Computers and Information in Engineering Conference (IDETC/CIE), Montreal, QC, Canada, 15–18 August 2010.
24. Jensen, B.D.; Howell, L.L. Bistable Configurations of Compliant Mechanisms Modeled Using Four Links and Translational Joints. *J. Mech. Des.* **2004**, *126*, 657–666. [CrossRef]
25. Chen, S.; Wang, M.Y. Designing distributed compliant mechanisms with characteristic stiffness. In Proceedings of the ASME 2007 International Design Engineering Technical Conferences and Computers and Information in Engineering Conference (IDETC/CIE), Las Vegas, NV, USA, 4–7 September 2007.
26. Lum, G.Z.; Teo, T.J.; Yeo, S.H.; Yang, G.; Sitti, M. Structural optimization for flexure-based parallel mechanisms—Towards achieving optimal dynamic and stiffness properties. *Precis Eng.* **2015**, *42*, 195–207. [CrossRef]
27. Howell, L.L.; Magleby, S.P.; Olsen, B.M. *Handbook of Compliant Mechanisms*; John Wiley & Sons: West Sussex, UK, 2013.
28. Howell, L.L.; DiBiasio, C.M.; Cullinan, M.A.; Panas, R.M.; Culpepper, M.L. A Pseudo-Rigid-Body Model for Large Deflections of Fixed-Clamped Carbon Nanotubes. *J. Mech. Robot.* **2010**, *2*, 034501. [CrossRef]
29. Su, H.-J. A Pseudorigid-Body 3R Model for Determining Large Deflection of Cantilever Beams Subject to Tip Loads. *J. Mech. Robot.* **2009**, *1*, 021008. [CrossRef]

30. Chen, G.; Xiong, B.; Huang, X. Finding the optimal characteristic parameters for 3R pseudo-rigid-body model using an improved particle swarm optimizer. *Precis Eng.* **2011**, *35*, 505–511. [CrossRef]
31. Teo, T.J.; Chen, I.-M.; Yang, G. A Large deflection and high payload flexure-based parallel manipulator for UV nanoimprint lithography: Part II. Stiffness modeling and performance evaluation. *Precis Eng.* **2014**, *38*, 872–884. [CrossRef]